Cytotherapy 23 (2021) 1097–1107

Contents lists available at ScienceDirect

CYTOTHERAPY

journal homepage: www.isct-cytotherapy.org

FULL-LENGTH ARTICLE
Translational Research

Amniotic fluid-derived extracellular vesicles: characterization and therapeutic efficacy in an experimental model of bronchopulmonary dysplasia

Michael A. Bellio[1,*], Karen C. Young[2], Julian Milberg[1], Ivan Santos[1], Zanub Abdullah[1], Danique Stewart[1], Alissa Arango[1], Pingping Chen[2], Jian Huang[2], Kevin Williams[2], Kaitlyn Kelly[2], Shanique Sterling[2], Aisha Khan[3], Xiumin Xu[3], George C. Shapiro[1], Maria Ines Mitrani[1]

[1] *Organicell Regenerative Medicine, Inc, Miami, Florida, USA*
[2] *Department of Pediatrics, University of Miami Miller School of Medicine, Miami, Florida, USA*
[3] *AssureImmune LLC, Miami, Florida, USA*

ARTICLE INFO

Article History:
Received 30 November 2020
Accepted 22 July 2021

Key Words:
amniotic fluid
bronchopulmonary dysplasia
extracellular vesicles
hyperoxia
lung injury
pulmonary

ABSTRACT

Background aims: Extracellular vesicles (EVs) are being tested for their use as novel therapeutics. However, the optimal source of EVs is currently under investigation. Amniotic fluid (AF) is a natural source of EVs that can be easily obtained for use in regenerative medicine, yet AF-EV characterization has not been fully explored.
Methods: Here the authors demonstrate AF as a rich source of EVs and identify the microRNA and proteomic cargo. Bioinformatics analysis of this cargo revealed multiple pathway targets, including immunomodulatory, anti-inflammatory and free radical scavenging networks. The authors further demonstrated the therapeutic potential of this EV product as a novel preventative agent for bronchopulmonary dysplasia (BPD).
Results: Intra-tracheal administration of AF-EVs preserved alveolar development, attenuated vascular remodeling and pulmonary hypertension, decreased lung pro-inflammatory cytokine expression and reduced macrophage infiltration in an experimental BPD model.
Conclusions: The authors' results suggest that AF is a viable biological fluid for EV harvest and that AF-EVs have strong therapeutic potential for pulmonary diseases, such as BPD, warranting further development to transition this novel EV product into the clinic.

Introduction

Over 15 million babies are born prematurely (<37 weeks' gestational age) every year, accounting for 6–14% of births worldwide [1,2]. According to the Centers for Disease Control and Prevention, the prematurity rate has worsened for the fourth consecutive year in the USA, and preterm complications are the main contributor to infant mortality [3]. Even more concerning is that almost 50 000 infants are born every year at less than 28 weeks' gestational age (extreme pre-term birth). Lifesaving interventions like early surfactant therapy have reduced neonatal mortality, but perinatal stressors [4] and suboptimal endogenous reparative responses have resulted in a myriad of complications, the most common of which is bronchopulmonary dysplasia (BPD) [2]. BPD (or chronic lung disease of prematurity) affects one in every three extreme pre-term infants, with an increasing incidence in the past 10 years [5]. The disease is characterized by an arrest of alveolar development, abnormal pulmonary vascular growth, excessively remodeled pulmonary vessels and, in the most severe cases, pulmonary hypertension (PH) and right heart failure [6]. Infants with BPD are also at greater risk of viral infections [7], recurrent hospitalizations, longer hospital stays, poor growth, cerebral palsy and long-term cardiopulmonary morbidities. Early treatment interventions are critical to mitigate the long-term morbidities of BPD.

Stem cell and other cell-based therapies have become increasingly popular as new interventions for BPD [8,9]. However, effective cell therapies have been slow to enter the clinic as a result of a number of logistical challenges, such as cell delivery, cell survival and reproducible large-scale manufacturing. In recent years, research has revealed that the beneficial effects of transplanted stem cells are mainly paracrine-mediated via the

* Correspondence: Michael A. Bellio, PhD, Organicell Regenerative Medicine, Inc, 1951 NW 7th Ave, Suite 300, Miami, Florida 33136, USA.
E-mail address: mbellio@organicell.com (M.A. Bellio).

https://doi.org/10.1016/j.jcyt.2021.07.011

release of extracellular vesicles (EVs) such as exosomes [10–12]. Therefore, EV-based therapies have gained traction as the newest generation of cell-derived biologic therapeutics.

EVs can be sourced from *in vitro* cell-conditioned media or from biological fluids for use as a therapeutic agent [13,14]. The collection of EV-rich biological fluids may supersede the need to manufacture *in vitro* cultured EV products and may surpass associated challenges. Amniotic fluid (AF) is an example of an easily obtainable biological fluid that is known to contain EVs [15,16]. AF is derived from the intrauterine environment and contains perinatal secreted nutrients, cytokines and growth factors, which support fetal development and maturation [17]. To date, characterization of the AF-EV fraction and its regenerative potential has not been fully explored.

Here the authors aimed to demonstrate that AF is a rich source of therapeutic EVs that can be used as a novel treatment for BPD. Furthermore, the authors hypothesized that AF-EVs are enriched with nucleotides and proteins that are anti-inflammatory and lung-protective. The authors show that AF-EVs contain a cargo of microRNAs (miRNAs) and proteins that modulate inflammation and oxidative stress, key contributors to BPD pathogenesis. The authors also demonstrate that intra-tracheal (IT) administration of AF-EVs preserves lung alveolar development, decreases pulmonary hypertension and reduces lung inflammation in rodents with experimental BPD. These findings have significant implications, as they suggest that AF-EVs are potential translational therapeutics for BPD.

Methods

AF-EV characterization

Isolation of AF-EVs

AF was collected from healthy donors during planned, full-term cesarean sections after obtainment of an institutional review board-approved protocol (Institute of Regenerative and Cellular Medicine IRB approval number, IRCM-2020-254). All donors signed informed consent forms for tissue to be used in research. The AF was centrifuged and processed with a proprietary filtration system to remove all cellular debris. EVs were precipitated from the processed AF via ultracentrifugation at 100 000 × g for 3 h at 4°C using a fixed-angle rotor and a Beckman Coulter (Brea, CA, USA) ultracentrifuge. The resulting pellet was then resuspended in sterile-grade 0.9% sodium chloride (normal saline).

NanoSight nanoparticle tracking analysis

Nanoparticle tracking analysis (NTA) was performed using a NanoSight NS300 instrument and NanoSight NTA 3.4 software, build 3.4.003 (Malvern Panalytical, Malvern, UK). After processing, AF-derived product was diluted 1:1000 in water. The diluted samples were then introduced to the NanoSight NS300 instrument. The capture settings were modified to capture 10 video files with a capture duration of 30 s using a camera level of 15 and a continuous syringe pump flow rate of 50. After completion of the script, the video files were analyzed with a detection threshold of 3. NTA post-acquisition settings were kept constant between samples and any video files that experienced uncorrected vibration and/or poor tracking analysis were excluded from the final analysis report.

Transmission electron microscopy

Isolated AF-EVs from three independent donors were analyzed using a JEOL JEM-1230 electron microscope (JEOL USA, Inc, Peabody, MA, USA) in conjunction with formvar carbon-coated transmission electron microscopy grids (FCF400-Cu; Electron Microscopy Sciences, Hatfield, PA, USA). The copper carbon formvar grids were glow-discharged prior to loading an undiluted sample of EVs. The grids were then floated on 10 μL of EV sample drop for 15 min, washed two times with water by floating on the drop of water for 30 s and then negatively stained with 2% uranyl acetate by floating on the drop of stain for 30 seconds. The grids were blot-dried with Whatman paper (Cytiva, Marlborough, MA, USA) and then imaged.

Fluorescent NTA

Fluorescent NTA (fNTA) was performed using a ZetaView QUATT with ZetaView software version 8.05.12 SP1 (Particle Metrix GmbH, Inning am Ammersee, Germany). Isolated AF-EVs were labeled with anti CD63-Alexa 488 (NBP2-42225AF488) and anti CD81-DyLight 550 (NB100-65805R) (Novus Biologicals, Littleton, CO, USA) by adding 1 μL of each fluorescent antibody to 20 μL of sample containing isolated EVs, and then the sample was vortexed for 5 s. The fluorescently labeled EV samples were then incubated for 2 h in the dark on ice. The samples were diluted by mixing deionized water filtered through a 0.2-μm syringe filter with corresponding volumes of sample. The fNTA was performed in scatter mode, 488/500 fluorescent mode and 520/550 fluorescent mode. For scatter mode analysis, the ZetaView settings were adjusted to have a sensitivity of 75, shutter speed of 100, cycles/positions of 2/11, frame rate of 30, maximum size of 1000, minimum size of 20, track length of 15 and minimum brightness of 20. Fluorescent mode analysis had similar parameters with the exception of an increased sensitivity of 80–85. The size and concentration profiles of each mode were then imported into Excel (Microsoft Corporation, Redmond, WA, USA) and superimposed. This experiment was repeated using three AF-EV preps isolated from different donors.

MACSPlex exosome surface marker analysis

A MACSPlex exosome kit (Miltenyi Biotec, Bergisch Gladbach, Germany) was used to detect 37 potential exosome surface markers on the isolated AF-EVs according to the manufacturer's instructions. In short, capture beads were added to the EVs and exosome detection reagent was used to detect CD63-, CD81- and CD9-expressing EVs. Various fluorescent bead populations were used to label the exosome surface markers. The fluorescence intensity of each marker was determined by flow cytometry analysis. Background fluorescence intensity was determined using isotype controls and subtracted from the median intensity of each marker. This experiment was repeated using three AF-EV preps isolated from different donors.

Thioredoxin 1 enzyme-linked immunosorbent assay

The concentration of thioredoxin 1 (TXN1) in AF-EV protein lysate was completed using an enzyme-linked immunosorbent assay (ELISA). AF-EV pellets were resuspended in Pierce RIPA buffer (Thermo Fisher Scientific, Waltham, MA, USA) with ChemCruz protease inhibitor cocktail (Santa Cruz Biotechnology, Inc, Dallas, TX, USA) followed by sonication for 5 s on ice a total of four times. Protein concentration was measured with a Pierce bicinchoninic acid protein assay. Total TXN1 concentration in the sample was measured using an ELISA kit (EH451RB; Thermo Fisher Scientific). Absorbance was measured using a SpectraMax ABS plate reader (Molecular Devices, San Jose, CA, USA)

miRNA sequencing of AF-EVs

AF-EVs collected from three donors were processed for miRNA isolation and sequencing in triplicate. The miRNA extraction and sequencing were conducted by QIAGEN Genomic Services (Germantown, MD, USA). RNA was isolated using part II of an exoRNeasy midi kit (QIAGEN) and automated on a QIAcube (QIAGEN). A total of 700 μL of QIAzol (QIAGEN) was added to the EVs, and then the authors continued with the second part of the exoRNeasy midi kit for RNA purification per the manufacturer's protocol. RNA, including RNA spike-ins in the purification step, was extracted from the samples to allow monitoring of the RNA extraction efficiency. Each RNA sample was successfully reverse-transcribed into complementary DNA (cDNA) and tested for the expression of five miRNAs and three synthetic spike-ins. RNA was reverse-transcribed in 10-μL reactions using a miRCURY LNA reverse transcription kit (QIAGEN). The cDNA was diluted 100× and assayed in 10-μL polymerase chain reactions

(PCRs) using a miRCURY LNA SYBR Green PCR kit (QIAGEN). The amplification was performed using a LightCycler 480 system (Roche Diagnostics, Basel, Switzerland) in 384-well plates. The amplification curves were analyzed using Roche LightCycler software, both for determination of Cq (by the second derivative method) and for melting curve analysis. Raw data were extracted from the Roche LightCycler software. The evaluation of expression levels was performed based on raw Cq values.

The library preparation was done using the QIAseq miRNA library kit (QIAGEN). A total of 5 μL of RNA was converted into miRNA next-generation sequencing libraries. Adapters containing unique molecular identifiers were ligated to the RNA, and then RNA was converted to cDNA. The cDNA was amplified using PCR (22 cycles), and indices were added during the PCR. After PCR, the samples were purified. Library preparation quality control was performed using either a Bioanalyzer 2100 or TapeStation 4200 (Agilent Technologies, Santa Clara, CA, USA). The library pool was then sequenced on a NextSeq 500 sequencing instrument (Illumina, Inc, San Diego, CA, USA) according to the manufacturer's instructions. Raw data were de-multiplexed and FASTQ files for each sample were generated using bcl2fastq software (Illumina, Inc). FASTQ data were checked using the FastQC tool. FASTQ data were processed in QIAGEN's OmicSoft array suite version 10.1.1.14. Following the pre-processing of the reads, reads were aligned to the genome using the OmicSoft sequence aligner. All statistical analysis and miRNA identification were performed by QIAGEN Genomic Services.

Proteomic analysis

AF-EVs collected from three donors were subjected to protein precipitation using a glacial acetone method. Cold acetone was added to samples in a 4:1 ratio. Samples were briefly vortexed and incubated overnight at −20°C. After incubation, samples were centrifuged at 15 000 × g at 4°C for 15 min. After centrifugation, the supernatants were removed and the protein pellets were washed with acetone. After washing, the pellets were allowed to air dry at room temperature. The pellets were reconstituted in 0.2 mL of 8 M urea. To complete protein digestion, 50 μg of protein was reduced with dithiothreitol, alkylated with iodoacetamide and subjected to overnight trypsin digestion. Peptide samples were cleaned with Pierce C18 desalting columns (Thermo Fisher Scientific) prior to peptide quantitation. Samples were analyzed by liquid chromatography with tandem mass spectrometry using an EASY-nLC 1200 with Q Exactive HF (Thermo Fisher Scientific) and normalized to the total peptide amount. Protein identification and quantification were completed using MaxQuant and the UniProt human database.

Bioinformatics

Bioinformatics was completed using Ingenuity Pathway Analysis (IPA) Knowledge Base software version 01-16 (QIAGEN). For miRNA analysis, mature miRNA and messenger RNA (mRNA) target relationships were determined. All gene targeting was limited to relationships with experimental observed findings. For protein analysis, the commonly expressed proteins identified from mass spectrometry were uploaded to create a protein database on IPA. Proteins and mRNA target lists were used for core analysis to identify canonical pathways, top functional groups and top networks. During core analysis, Fisher's exact test is used to calculate the statistical significance of overlap of the data set molecules with various sets of molecules that represent annotations such as canonical pathways, upstream regulators and diseases. The test looks at the number of molecules in the chosen reference set and determines which are eligible for such analysis. In the right-tailed Fisher's exact test, only over-represented annotations—those that have more analysis-ready molecules than expected by chance—are significant. Under-represented annotations ("left-tailed" *P*values), which have significantly fewer molecules than expected by chance, are not shown.

The *P*values are calculated using the reference set that is defined in the settings on the Create Analysis page. By using the unfiltered data set as the reference set, the resulting *P*values indicate how significant the molecule overlap is with each annotation considering both the molecules assayed (reference set) and the input molecules that met the cutoff (analysis-ready molecules). Venny 2.1 was used to create Venn diagram comparison charts.

Pathway analysis to identify predicted miRNA–RNA interactions was completed using the IPA Knowledge Base software version 01-16 bioprofiler and pathway tools. To complete this search, bioprofiler analysis created a data set of genes associated with respiratory system inflammation. This list was filtered to include only those genes targeted by the AF-EV miRNAs. The list was further filtered to include only genes in which increased activity has been associated with increased respiratory inflammation. Using the generated list, the pathway tool was used to identify the direct (human) miRNA–RNA targeting interactions with experimentally observed relationships.

Experimental BPD and PH model

Animal maintenance

Pregnant Sprague Dawley rats were purchased from Charles River Laboratories (Wilmington, MA, USA). Rats were treated according to National Institutes of Health guidelines for the use and care of laboratory animals following approval of the study protocol by the University of Miami Animal Care and Use Committee.

Experimental BPD model

Newborn Sprague Dawley rats were assigned to normoxia (21% oxygen, room air) or hyperoxia (85% oxygen) from postnatal day (P) 1 to P14. Oxygen exposure was achieved in a plexiglass chamber using a flow-through system, and the oxygen level inside the chamber was monitored daily with a Maxtec oxygen analyzer (OM25-RME; Maxtec, Salt Lake City, UT, USA). Mother rats were rotated every 48 h between hyperoxia and normoxia chambers to prevent damage to their lungs. Litter size was adjusted to 10–12 pups to control for the effect of litter size on nutrition and growth. Right ventricular systolic pressure (RVSP) measurements, right ventricular hypertrophy and lung morphometric and molecular studies were performed at P14.

AF-EV administration

Newborn rats exposed to normoxia or hyperoxia from P1 to P14 were given a single IT injection of 1×10^{10} total AF-EVs suspended in 50 μL of saline or 50 μL of saline only (placebo) on P3 (preventative approach) or P7 (therapeutic approach).

Hemodynamic studies

Following normoxic and hyperoxic exposures, rats were evaluated at P14. Rats were anesthetized with 1% isoflurane and RVSP was measured as previously described [18]. Briefly, after thoracotomy, a 25-gauge needle fitted to a pressure transducer was inserted into the right ventricle. RVSP was measured and continuously recorded on a Gould polygraph (TA-400; Gould Instrument Systems, Inc, Cleveland, OH, USA). Immediately after RVSP measurements were obtained, the animals were killed. Right ventricular hypertrophy was determined by measuring the weight ratio of the right ventricle (RV) to the left ventricle (LV) and septum (S) (RV/(LV+S)).

Lung morphometric analysis

Lungs were perfused and fixed in 4% paraformaldehyde and embedded in paraffin. Serial sections, 5-μm thick, were taken from the upper and lower lobes and stained with hematoxylin and eosin. Images from five randomly selected, non-overlapping parenchymal fields were acquired from lung sections of each animal using an Olympus Q-Color3 (Olympus America, Inc., Melville, NY, USA) color

camera interfaced with a light microscope (DMI 4000B; Leica, Wetzlar, Germany) at 20× magnification. Alveolarization was determined by calculating the mean linear intercept (MLI). MLI was calculated by determining the average distance between intersects of alveolar septal tissue and a superimposed counting grid. Images were analyzed using ImageJ version 1.53a.

Pulmonary vascular density

Lung sections were deparaffinized, rehydrated and stained with polyclonal rabbit anti-human von Willebrand factor 1:50 (Dako North America, Inc, Carpinteria, CA, USA). The number of vessels (diameter, 20–50 μm) per high-power field (HPF) was quantified in five randomly selected, non-overlapping parenchymal fields from lung sections of each animal. Images from non-overlapping parenchymal fields were acquired from lung sections of each animal using an Olympus Q-Color3 color camera interfaced with a Leica light microscope at 20× magnification. Images were analyzed using ImageJ version 1.53a.

Pulmonary vascular remodeling

Paraffin-embedded sections were stained with polyclonal rabbit anti-human von Willebrand factor and monoclonal mouse anti-alpha smooth muscle actin 1:500 (Sigma-Aldrich, St Louis, MO, USA). The percentage of peripheral pulmonary vessels (<50 μm in diameter) stained with anti-alpha smooth muscle actin over >50% of the circumference was determined from 10 random images of each lung section, and all analyses were performed by a blinded observer. Images from non-overlapping parenchymal fields were acquired from lung sections of each animal using an Olympus Q-Color3 color camera interfaced with a Leica light microscope at 20× magnification. Images were analyzed using ImageJ version 1.53a.

Pulmonary macrophage infiltration

Lung macrophage infiltration was assessed by immunostaining lung sections with a rat monoclonal antibody to MAC-3 at 1:20 (BD Biosciences, San Jose, CA, USA). The number of MAC-3+ cells in the alveolar air spaces was determined by evaluating six random HPFs on each slide and quantifying the number of MAC-3+ cells per HPF. Images from non-overlapping parenchymal fields were acquired from lung sections of each animal using an Olympus Q-Color3 color camera interfaced with a Leica light microscope at 20× magnification. Images were analyzed using ImageJ version 1.53a.

Lung inflammatory cytokine mRNA expression

IL-1α, IL-1β, MCP-1 and MIP-1α gene expression was determined by real-time PCR. RNA from P14 rat lung tissue was extracted (miRNeasy mini kit; QIAGEN) and reverse transcription performed (GoScript reverse transcription kit; Promega Corporation, Madison, WI, USA). The real-time PCR reaction was completed using SsoAdvanced Universal SYBR Green supermix (Bio-Rad Laboratories, Hercules, CA, USA) on an ABI Fast 7500 system (Applied Biosystems, Foster City, CA, USA). Primers for IL-1α, IL-1β, MCP-1, MIP-1α and β-actin (as an internal control) were obtained from Sigma-Aldrich. The relative mRNA expression of IL-1α, IL-1β, MCP-1 and MIP-1α was normalized to β-actin expression and the fold change calculated from gene expression in the room air (RA)–placebo (PL) group. Gene primer design was as follows: IL-1α forward (5′ -> 3′) GCATCCTCAGCAGCAGAATT, reverse (5′ -> 3′) ACAGGAGGGCAAAAGACTGA; IL-1β forward (5′ -> 3′) TTGAGTCTGCACAGTTCCCC, reverse (5′ -> 3′) GTCCTGGGGAAGGCATTAGG; MCP-1 forward (5′ -> 3′) AGCCAACTCTCACTGAAGCC, reverse (5′ -> 3′) AACTGTGAACAACAGGCCCA; MIP-1α forward (5′ -> 3′) CGAAGTCTTCTCAGCGCCATA, reverse (5′ -> 3′) TGGAATTTGCCGTCCATAGG; β-actin forward (5′ -> 3′) GCAGGAGTACGATGAGTCCG, reverse (5′ -> 3′) ACGCAGCTCAGTAACAGTCC.

Statistical analysis

Data are expressed as mean ± standard deviation and were analyzed by two-way analysis of variance with post-hoc analysis (Tukey). $P \leq 0.05$ was considered statistically significant. Figures were created and statistical analysis performed using Prism 9 software (GraphPad Software, San Diego, CA, USA)

Results

Nanoparticle composition of amniotic fluid

Nanoparticle size composition and distribution of the processed AF were measured using NTA (Figure 1A). The analysis found AF to contain an average of $2.3 \times 10^{11} \pm 1.68 \times 10^{8}$ particles per mL with a mode size of 101.2 ± 3.8 nm (Figure 1B,C). Transmission electron microscopy images revealed a "deflated" balloon phenotype of the EVs that was within the expected size range of <200 nm (Figure 1D).

Characterization of AF-EV particles

Positive EV identification was completed using fNTA to demonstrate positive expression of transmembrane proteins CD63 and CD81 (Figure 2A,B). Comparison of unstained and stained particles revealed that the nanoparticles were 69.4 ± 6.4% positive for CD63 and 70.8 ± 4.8% positive for CD81 (Figure 2C). Multiplex analysis of exosome surface markers further revealed positive detection of exosome-associated markers (CD9, CD81 and CD63) (Figure 2D). This analysis also identified several other protein markers that were present on AF-EVs at various intensity levels (CD14, CD24, CD44, CD326 and CD133).

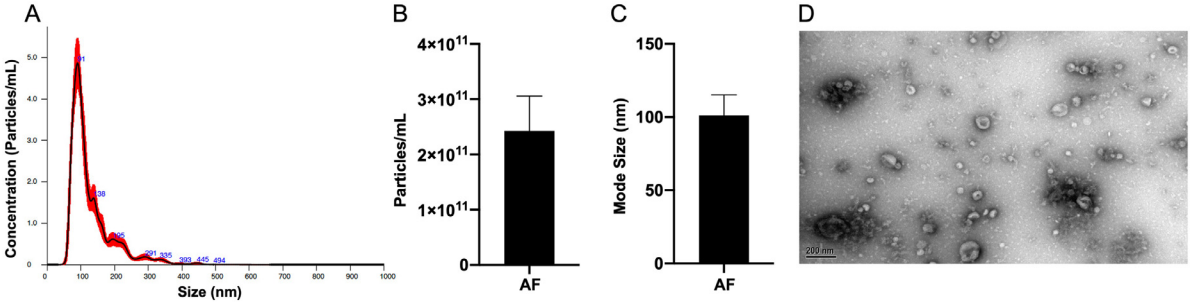

Figure 1. Nanoparticle analysis of AF (amniotic fluid). (A) NTA and size distribution analysis of processed AF. (B) Average particle per mL concentration of processed AF (n = 14). (C) Average of the mode particle size (nm) of processed AF (n = 14). (D) Representative TEM image of nanoparticles isolated from processed AF. Error bars represent standard error of the mean. TEM, transmission electron microscopy.

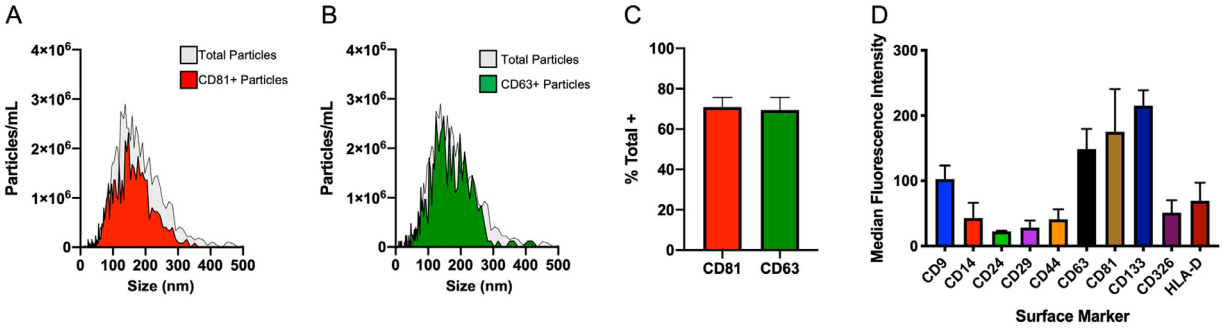

Figure 2. Nanoparticle surface marker characterization. (A) fNTA of CD81+ particles compared with total unstained particles. (B) fNTA of CD63+ particles compared with total unstained particles. (C) Average percentage of CD81+ and CD63+ particles (n = 3). (D) Median fluorescence intensity of positively detected EV- and exosome-associated markers (n = 3). Error bars represent standard error of the mean.

Sequencing EV miRNA cargo

The miRNA sequencing was completed on EVs isolated from three different donors and detected 102 commonly expressed miRNAs above 100 copies (Figure 3A; also see supplementary Table 1). The top 50 miRNAs were listed in descending order of expression, from highest to lowest expression. The top five most concentrated miRNAs were let-7b, miR-200c, miR-30d, miR-125a and miR-483 (Figure 3B). Interestingly, the top 15 concentrated miRNAs accounted for 80% of the total miRNA content (Figure 3C). Bioinformatics analysis was performed using the Qiagen IPA software to identify 81 mature miRNAs from the 102 sequenced miRNAs. Of the 81 mature miRNAs, 63 were linked to 1216 different mRNAs (with experimentally observed relationships). The identified mRNAs were further analyzed using IPA top canonical pathway analysis to reveal the top pathways associated with the targeted mRNAs (Figure 3D). The top pathways identified included macrophage recruitment and invasion, senescence, IL-6 signaling, osteoarthritis and nuclear factor-kB signaling.

Bioinformatics analysis was also performed to predict miRNA–RNA interactions on genes associated with respiratory system inflammation. This analysis identified 14 miRNAs that directly target an array of genes (see supplementary Table 2), and miR-146a-5p, one of the top miRNAs identified in AF-EVs, was predicted to directly interact with 16 different genes associated with respiratory system inflammation.

Protein analysis of EV cargo

Mass spectrometry analysis of AF-EV preparations identified 315 commonly expressed proteins (Figure 4A). Among the diverse collection of proteins, this analysis detected several exosome marker proteins,

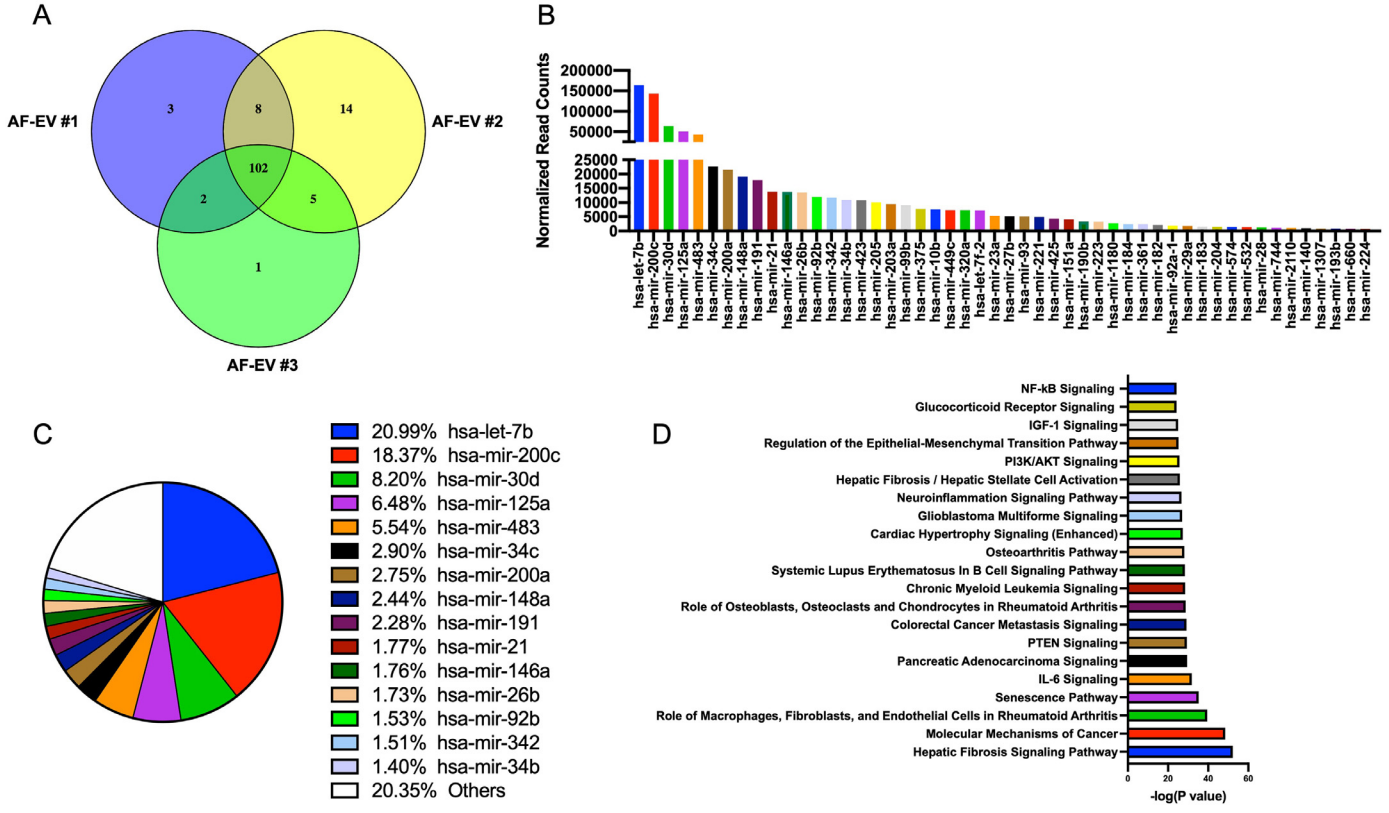

Figure 3. miRNA sequencing and bioinformatics of AF-EV cargo. (A) Venn diagram analysis of commonly expressed miRNAs above 100 copies (n = 3). (B) Normalized read count of the top 50 expressed miRNAs. (C) Pie chart analysis of the top 15 expressed miRNAs compared with the remaining content. (D) Top 21 canonical pathways identified from bioinformatics analysis of the RNA targets corresponding to the miRNA cargo. NF-kB, nuclear factor-kB; PTEN, phosphatase and tensin homolog.

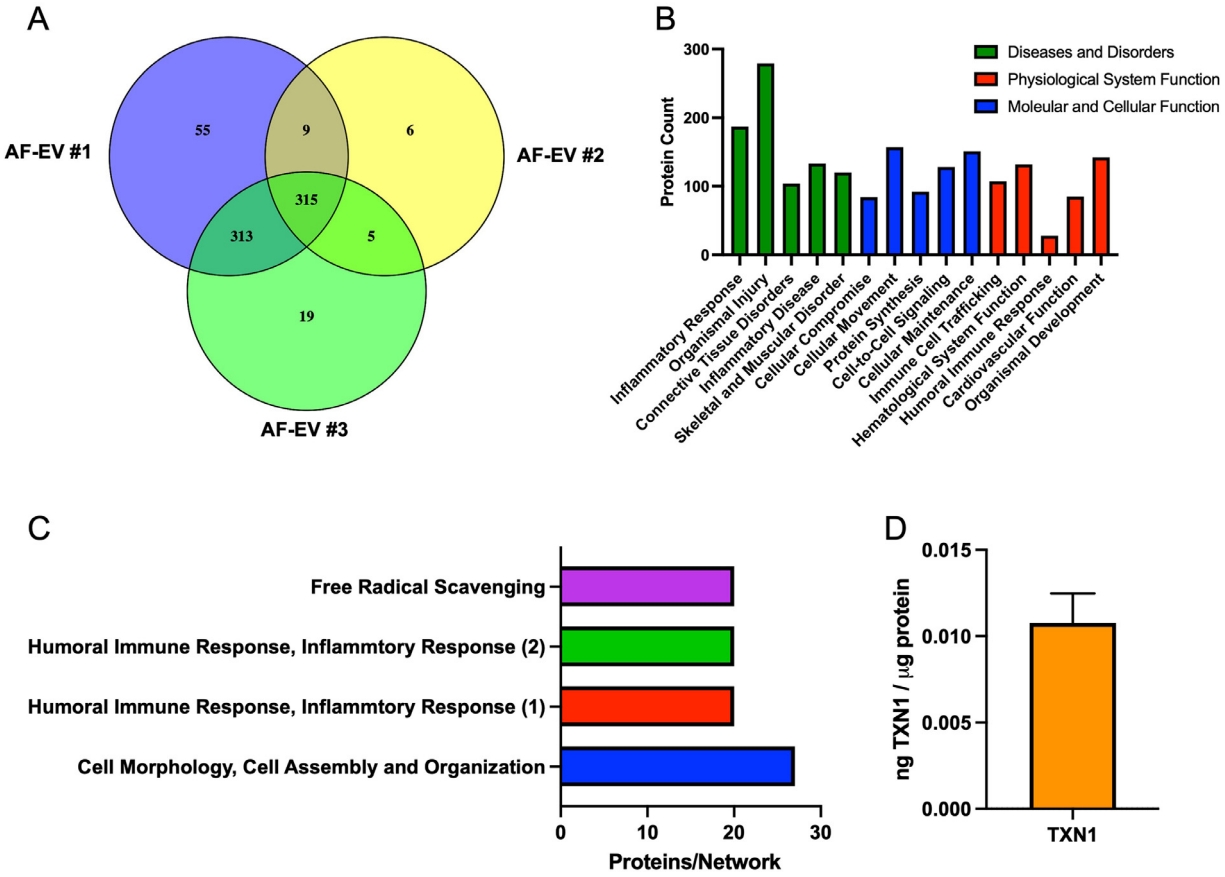

Figure 4. Proteomic and bioinformatics of AF-EV cargo. (A) Venn diagram analysis of commonly expressed proteins (n = 3). (B) Top diseases and disorders, physiological system functions and molecular and cell functions identified from the commonly expressed protein list based on the number of identified molecules in each category. (C) Top four protein networks identified from the commonly expressed protein list by the total number of focus molecules detected. (D) Quantification of TRX concentration in AF-EV protein lysate (n = 5).

including CD8, CD9, flotillin-1 and TSG101, along with various heat shock proteins and annexin (see supplementary Tables 3, 4). Bioinformatics analysis of the protein cargo determined top disease and biofunction clusters (Figure 4B) The top diseases and disorder functions included inflammatory response, organismal injury and connective tissue disorders. The top physiological system functions included immune cell trafficking, hematological system function and humoral immune response. The top molecular and cellular functions identified included cellular

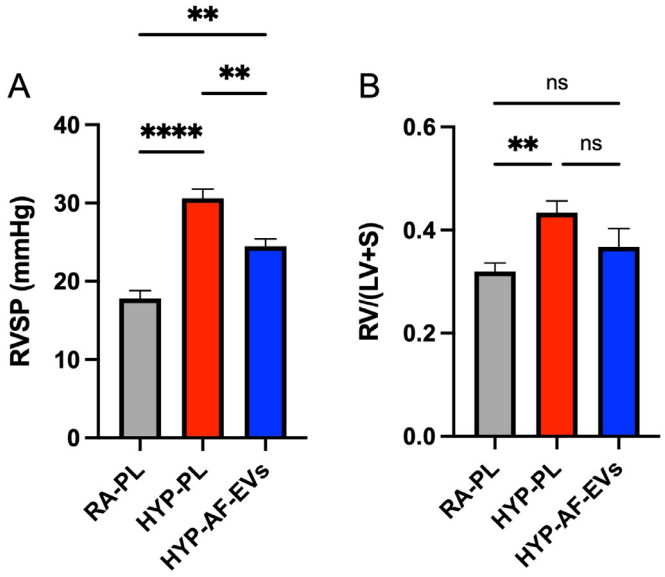

Figure 5. Effect of AF-EV administration on pulmonary hypertension and right ventricular hypertrophy. (A) Right ventricular systolic pressure (RVSP, mmHg) measurement in RA-PL, HYP-PL and HYP-AF-EV groups (n = 5–7 per group). (B) Right ventricular hypertrophy determined by mass of right ventricle (RV) divided by left ventricle (LV) and septum (S) (RV/(LV+S) in RA-PL, HYP-PL and HYP-AF-EV groups (n = 6–9 per group). Error bars represent standard error of the mean. ns $P > 0.05$, $^{**}P < 0.01$, $^{****}P < 0.0001$.

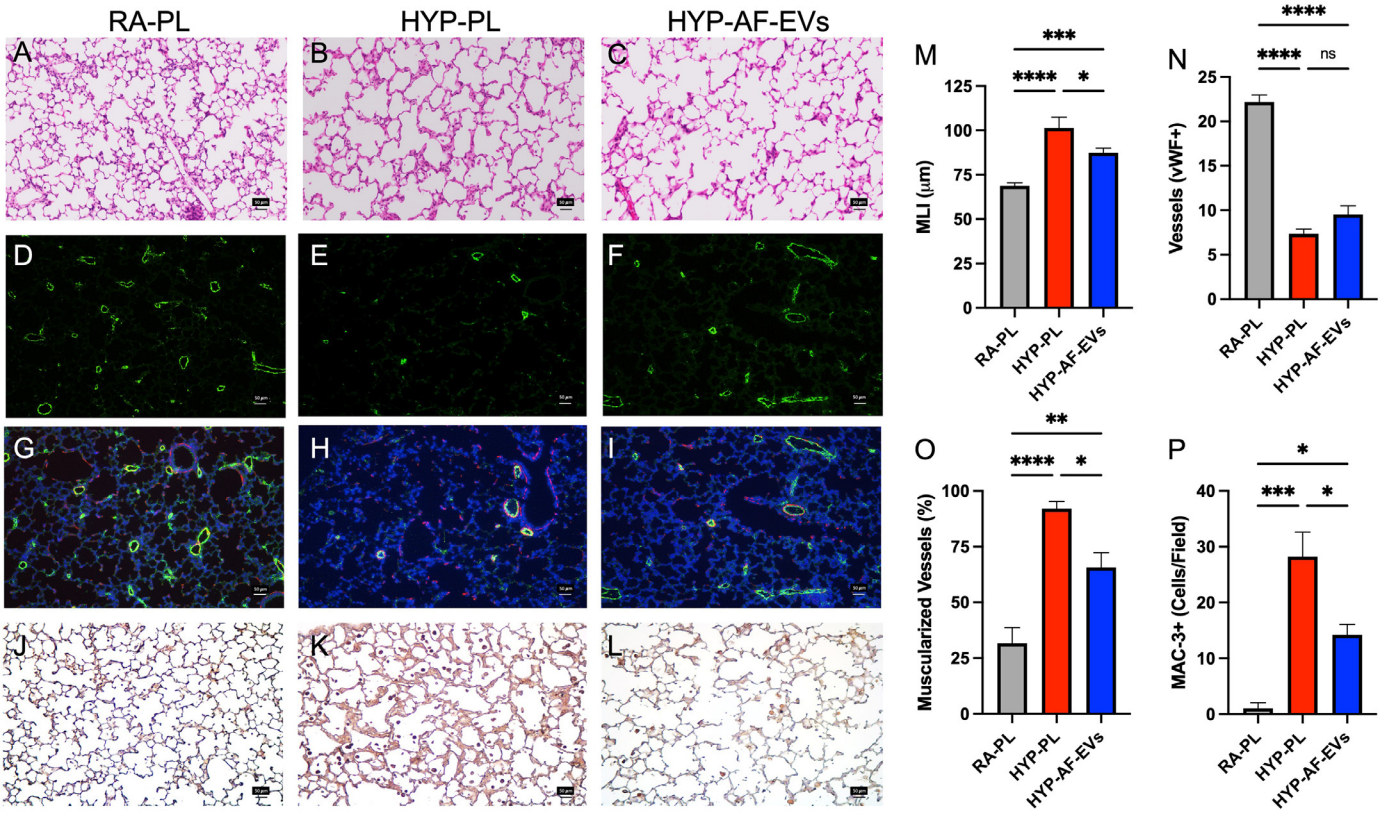

Figure 6. Effect of AF-EV administration on lung structure and macrophage infiltration. (A–C) Representative lung sections showing alveolar structure in each experimental group. (D–F) Representative immunofluorescent staining showing vWF+ immunostaining (green) in each experimental group. (G–I) Representative immunofluorescent staining of lung sections showing pulmonary vascular muscularization in each experimental group. Green = vWF, red = alpha smooth muscle actin. (J–L) Representative lung sections immunostained with macrophage marker MAC-3 antibody (brown) in each experimental group. (M) Quantification of MLI in each group (n = 4–7 per group). (N) Average vascular density quantification per field in each group (n = 6 per group). (O) Quantification of average percentage of muscularized vessels per field in each group (n = 5–6 per group). (P) Quantification of average number of MAC-3+ cells in all groups (n = 4–5 per group). Image magnification is ×20. Error bars represent standard error of the mean. ns $P > 0.05$, $^{*}P < 0.05$, $^{**}P < 0.01$, $^{***}P < 0.001$, $^{****}P < 0.0001$. vWF, von Willebrand factor.

movement, cell-to-cell signaling and cellular maintenance. Finally, the top four molecular networks identified from the protein list included cell morphology, two humoral immune response networks and free radical scavenging (Figure 4C). To confirm the expression of one of the identified free radical scavenging proteins, TXN1, ELISA analysis of AF-EV protein lysate was completed to obtain a value of 0.011 ng TXN1 protein/μg of total AF-EV protein (Figure 4D).

Therapeutic efficacy of AF-EVs in a pre-clinical BPD model

IT administration of AF-EVs was found to be safe, with no observation of adverse events. At P14, animals treated at P3 were assessed for pulmonary hypertension and right ventricular hypertrophy. AF-EV-treated animals had significantly decreased pulmonary hypertension, as seen by decreased RVSP (Figure 5A). RVSP increased in PL-treated,

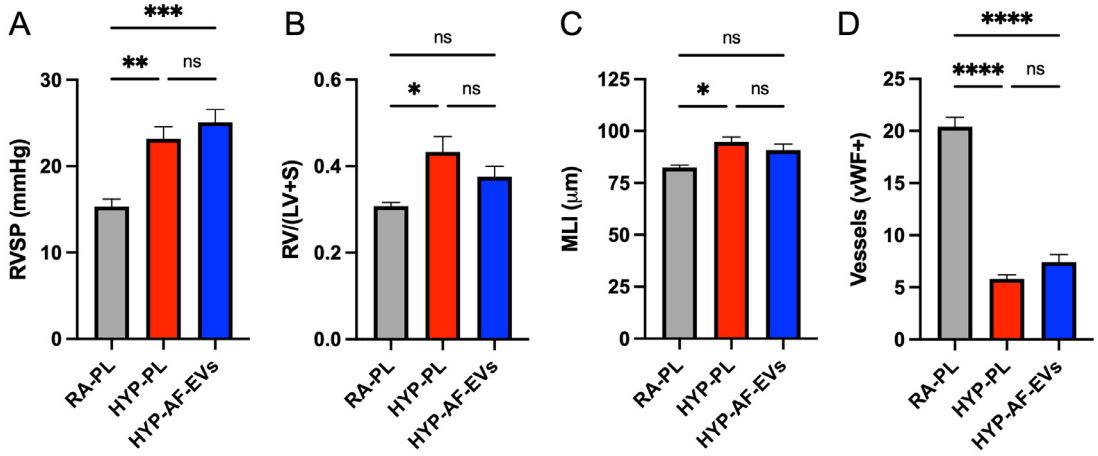

Figure 7. Effect of late AF-EV administration on experimental BPD and PH. (A) Right ventricular systolic pressure (RVSP) measurement in RA-PL, HYP-PL and HYP-AF-EV groups (n = 6–11 per group). (B) RV hypertrophy determined by weight of right ventricle (RV) divided by left ventricle (LV) and septum (S) (RV/(LV+S)) in RA-PL, HYP-PL and HYP-AF-EV groups (n = 4–10 per group). (C) Quantification of mean linear intercept (MLI)_ in each group (n = 4–5 per group). (D) Average vascular density quantification per field in each group (n = 5–6 per group). Error bars represent standard error of the mean. ns $P > 0.05$, $^{*}P < 0.05$, $^{**}P < 0.01$, $^{***}P < 0.001$, $^{****}P < 0.0001$.

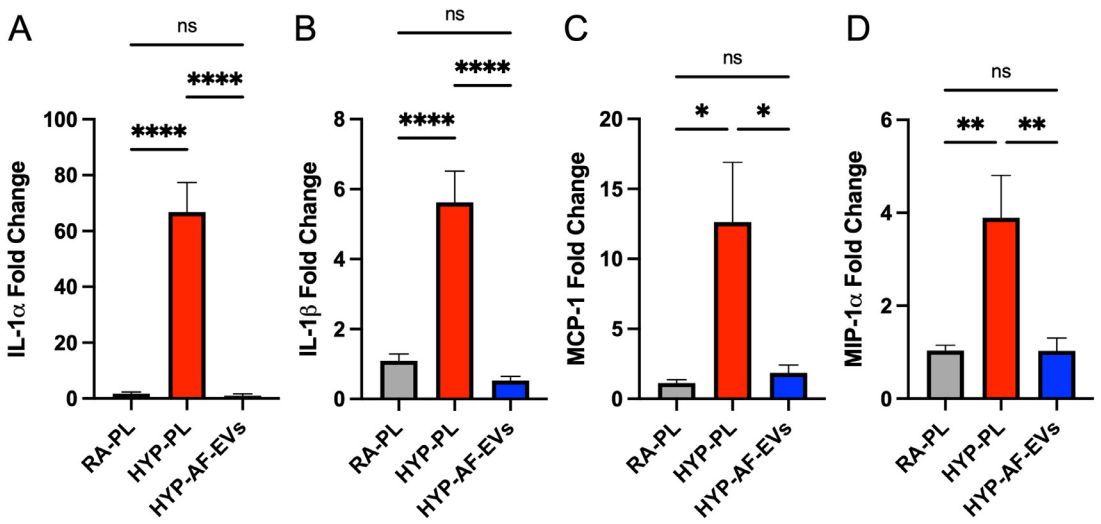

Figure 8. Effect of AF-EV administration on inflammatory cytokines. (A) Fold change of IL-1α RNA expression in each group relative to RA-PL group. (B) Fold change of IL-1β RNA expression in each group relative to RA-PL group. (C) Fold change of MCP-1 RNA expression in each group relative to RA-PL group. (D) Fold change of MIP-1α RNA expression in each group relative to RA-PL group (n = 6 per group). Error bars represent standard error of the mean. ns $P > 0.05$, $^{*}P < 0.05$, $^{**}P < 0.01$, $^{****}P < 0.0001$.

hyperoxia-exposed (HYP) animals (30.6 ± 1.16 mmHg) compared with PL-treated RA control (17.8 ± 1.02 mmHg) ($P < 0.0001$). This effect was significantly diminished in the HYP group that received AF-EV treatment (24.5 ± 0.93 mmHg, $P < 0.01$). Similarly, right ventricular hypertrophy increased in the HYP group that received PL (0.43 ± 0.02) compared with the RA-PL group (0.32 ± 0.02) ($P < 0.01$). Although there was a trend for reduced right ventricle/left ventricle and septum in the HYP group that received AF-EVs, right ventricular hypertrophy was not significantly different from either the RA-PL or HYP-PL group (Figure 5B).

Histological analysis of lung tissue revealed improved alveolar structure in the HYP group that received AF-EV treatment. Morphometric analysis revealed a significant reduction in MLI in the HYP group that received AF-EV treatment (87.4 ± 2.5 μm) compared with the HYP-PL group (101 ± 6.1 μm) ($P < 0.05$) (Figure 6A–C,M). Vascular density also decreased in the HYP-PL group (7.33 ± 0.6 vessels per HPF) compared with the RA-PL group (22.2 ± 0.8 vessels per HPF) ($P < 0.0001$). Vascular density in the HYP group did not, however, significantly increase with AF-EV treatment (9.5 ± 1.0 vessels per HPF) (Figure 6D–F,N). Pulmonary vascular remodeling was assessed by quantifying the percentage of muscularized vessels. Animals in the HYP-PL group had significantly increased pulmonary vascular remodeling (92.0 ± 3.3% muscularized pulmonary vessels) compared with the RA-PL group (31.33 ± 7.1% muscularized pulmonary vessels) ($P < 0.0001$). AF-EV treatment significantly reduced muscularization compared with the HYP-PL group (65.7 ± 6.6% muscularized pulmonary vessels, $P < 0.05$) (Figure 6G–I,O).

Immune response to the hyperoxia injury was measured by macrophage infiltration into lung tissue via MAC-3 immunostaining. Macrophage infiltration increased in response to hyperoxia in the HYP-PL group (28.2 ± 4.4 MAC-3+ cells per HPF) compared with the RA-PL group (0 ± 1.0 MAC-3+ cells per HPF) ($P < 0.001$). HYP animals that received AF-EV, however, had significantly reduced macrophage infiltration (14.20 ± 4.4 MAC-3+ cells per HPF) compared with the HYP-PL group ($P < 0.05$) (Figure 6J–L,P).

To assess whether AF-EVs had beneficial effects in established BPD, they were also administered in the same model at P7, and animals were analyzed for therapeutic efficacy at P14. Treatment at this later time point did not result in decreased pulmonary hypertension (RVSP) or reduction in right ventricular hypertrophy within the HYP-AF-EV group (Figure 7A,B). Similarly, there was no significant improvement in alveolar structure or vessel density in the HYP-AF-EV group compared with the HYP-PL group (Figure 7C,D).

Modulation of inflammatory cytokines

In animals treated with AF-EV at P3, lung tissue was collected at P14 for RNA expression analysis of inflammatory cytokines. IL-1α expression was significantly elevated by 67.0 ± 10-fold in the HYP-PL group compared with the RA-PL group ($P < 0.0001$). Expression of IL-1α was significantly reduced in the HYP-AF-EV group to 1.06 ± 0.6-fold ($P < 0.0001$) (Figure 8A). Similarly, IL-1β, MCP-1 and MIP-1α expression was significantly elevated in the HYP-PL group compared with the RA-PL group by 5.62 ± 0.9-fold ($P < 0.0001$), 12.6 ± 4.3-fold ($P < 0.05$) and 3.89 ± 0.9-fold ($P < 0.01$) and was significantly suppressed in the HYP-AF-EV group to 0.53 ± 0.1-fold ($P < 0.0001$), 1.87 ± 0.6-fold ($P < 0.05$) and 1.03 ± 0.3-fold ($P < 0.01$), respectively (Figure 8B–D).

Discussion

EV-based therapeutics have quickly emerged as a promising therapeutic candidate because of their anti-inflammatory and tissue regenerative effects shown across various pre-clinical models, including myocardial infarction, stroke and wound healing [19–21]. The authors' present study has demonstrated for the first time that AF-EVs are a potential drug candidate for BPD, as AF-EVs preserve alveolar structure, reduce pulmonary vascular remodeling, prevent pulmonary hypertension and significantly reduce the induction of inflammatory cytokines. Furthermore, characterization of AF-EVs has broadened our understanding of the therapeutic potential of this EV source.

This study demonstrates AF as a rich source of EVs and confirms the authors' hypothesis that AF-EVs are packaged with miRNA and protein cargo that may provide therapeutic relief in BPD. Previous studies have examined the therapeutic effect of EVs such as mesenchymal stromal cell (MSC)-derived EVs in the treatment of BPD. In these models, early administration of MSC-EVs ameliorated features of BPD, as seen by improvement in alveolar simplification, increased vascular density and overall prevention of pulmonary hypertension [22]. Additionally, late administration of MSC-EVs at P18 in a similar model of established BPD improved affected pulmonary parameters 10 days later. Together, these models demonstrated MSC-EV-mediated prevention and reversal of BPD pulmonary parameters [23].

Immunomodulation of macrophages and reduction in inflammation are underlying mechanisms of these protective effects [24]. Although MSC-EV pre-clinical results have been promising, these therapies require *in vitro* cell expansion of a single cell source to manufacture cell numbers large enough to isolate sufficient concentrations of EVs. This strategy imposes serious limitations on large-scale clinical development and commercialization of EV-therapeutics [25]. Lengthy cell culture expansion is costly in terms of reagents, labor and final product testing. Not only does the final EV product require testing, but the cell source material also needs extensive quality assurance testing, such as karyotyping and adenovirus testing [26,27]. Furthermore, the mass production of primary cell lines results in bulk quantities of EV-rich conditioned media that require downstream processing and handling. Depending on conditioned media concentrations, the purified EV concentrations will vary, with unknown clinical dose quantities. The authors' finding that AF contains a pool of harvestable EVs eliminates many of the challenges associated with traditional EV production. Large volumes of AF can be readily collected from healthy donors in planned, full-term cesarean section and can be repurposed through processing for therapeutic use.

The authors found AF to be a reproducible source of EV dose production. Processed AF contains EV concentrations of approximately 2.0×10^{11} particles per mL. Based on the authors' fluorescent nanoparticle tracking results, 70% of these nanoparticles are positive for the exosome markers CD63 and CD81, indicating a preservation of greater than 1.0×10^{11} exosomes per mL. Effective large animal EV doses have been shown to range from 1×10^{11} particles per dose to 3×10^{12} particles per dose [20,28,29], thus indicating that as little as 1 mL of AF is needed to obtain a clinically effective dose of EVs.

AF cellular components are largely heterogeneous and include cells derived from the fetus and fetal membrane. Therefore, the precise cellular origin of these EVs is likely to be mixed. Interestingly, the authors found that AF-EVs had high expression of CD133. The amniotic membrane is composed of epithelial and MSC populations. Characterization of these two cell types revealed amnion epithelial cells to express CD133 [30]. Interestingly, CD133+ AF-derived cells, isolated and expanded in culture, have been shown to be therapeutic, and EVs shed from these cells were found to be a primary source of the cell's regenerative effects [31,32]. Therefore, the positive detection of CD133 in the EVs opens up the possibility of epithelial cell origin and may represent a therapeutic component of cell types isolated from AF [33]. However, the wide range of cell types within the perinatal tissue environment, including placental trophoblasts, and fetal secretions that contribute to the pool of EVs must be acknowledged. Therefore, reproducibility of the harvested AF-EV populations needs to be considered in large-scale translation.

The regenerative potential of EVs and exosomes is derived from the intra-exosome molecular cargo. Mechanistic studies within animal models have revealed that the transfer of miRNA contributes to target cell gene expression changes and the induction of immunomodulatory effects [34–37]. The authors' completed analysis revealed the top miRNA content that may contribute to gene expression changes. The authors' analysis sequenced 102 unique miRNAs above 100 copies. This diverse collection of miRNAs has potentially thousands of gene targets involved in multiple pathways. Of note, the authors' bioinformatics analysis identified top canonical pathway targets, including general pro-inflammatory cascades such as the pro-inflammaory role of macrophages in rheumatoid arthritis, IL-6 signaling and nuclear factor-kB signaling. These pathways included gene targets such as interleukins, WNT family members, and tumor necrosis factor alpha. Comparison of this result with previously published miRNA sequencing of other EV types allows for the determination of unique miRNA cargo in AF-EVs. One example is the high expression of miR-146a in AF-EV compared with no expression in a bone marrow MSC-derived EV preparation [34]. However, this comparison is cell-source dependent, as similar miR-146a counts were described in an adipose MSC-derived EV preparation [38].

Similarly, proteomic analysis revealed potential therapeutic mediators. This analysis confirmed the presence of exosome-associated proteins such as tetraspanins (CD63, CD81 and CD9), annexin, heat shock proteins and other endosome-associated proteins such as TSG101. Pathway analysis of the protein list identified several key pathways of interest, including inflammatory response, immune modulation and free radical scavenging. Further review of the protein cargo revealed well-known antioxidant proteins, TXN1, glutathione S-transferase (GSTP1) and superoxide dismutase (SOD3). TXN1 is a small redox protein that promotes the programing of anti-inflammatory macrophages and attenuates hyperoxia lung injury by suppressing macrophage infiltration [39,40]. Furthermore, overexpression of SOD3 in murine models of BPD has demonstrated the key role of SOD3 in protecting against neonatal hyperoxia-induced alveolar damage [41].

The authors showed that administration of AF-EVs is a novel therapeutic strategy for the prevention of pulmonary hypertension and BPD. IT administration of AF-EVs in the early stages of disease, at P3, decreased pulmonary hypertension, preserved alveolar structure, reduced vascular remodeling and suppressed lung inflammation. Administration of AF-EVs at P7, where disease is established, was not sufficient to reverse the effects of established BPD. Therefore, under the authors' tested protocol, AF-EVs were only effective as a preventative agent and did not reverse established disease. However, this lack of therapeutic effect may be due to inadequate dosing or a shorter recovery time. More fine-tuning of the therapy may be needed to reverse an established injury.

AF-EV administration also suppressed the induction of pro-inflammatory cytokine expression that was the result of neonatal hyperoxia injury. RNA expression of IL-1α, IL-1β, MCP-1 and MIP-1α was suppressed in P14 rat lungs to a level similar to that seen in the RA-PL group. Increased pro-inflammatory signaling is a key feature of BPD, and it is well documented that cytokines released by activated fetal lung macrophages disrupt airway morphogenesis [42] and pre- or post-natal inflammation decreases alveolar septation [43]. Although it is difficult to predict which of the specific AF-EV cargo contribute to the therapeutic effect, the authors postulate that the improvement in lung structure and function seen following AF-EV administration is secondary to the reduction in lung inflammation induced by hyperoxia injury. Using bioinformatics and literature searches, the authors identified miR-146a as a potential mechanistic candidate. The treatment of B cells and airway smooth muscle cells with a miR-146a mimic has been shown to downregulate IL-1β and other inflammatory cytokines, such as IL-6 and IL-8 [44,45]. Interestingly, nanoparticle delivery of miR-146a has been proven to effectively inhibit pro-inflammatory cytokine secretion in a mechanically induced model of acute respiratory distress syndrome, further indicating the therapeutic potential of the miRNA in AF-EVs [46]. Collectively, the authors demonstrate that AF-EV cargo has lung protective effects through the downregulation of pro-inflammatory cytokines and chemokines, which may be efficacious for BPD and other adult diseases characterized by excessive inflammatory responses.

Conclusions

The authors' work demonstrates that AF contains EVs that can be harnessed for use in allogeneic drug development and that have beneficial effects in experimental BPD and PH. Moreover, AF-EVs possess anti-inflammatory properties that may contribute to the rescue seen with regard to lung structure and pulmonary hypertension. This work strengthens the clinical potential of AF-EVs as a novel EV source that may be rapidly translated into the clinic.

Funding

No funding was received.

Declaration of Competing Interest

MB, JM, IS, ZA, DS, AA, GS and MM are employees of Organicell Regenerative Medicine, Inc. MM is the chief science officer, serves on the Organicell Regenerative Medicine Board of Directors and holds equity in the company. AK and XX are 100% owners of AssureImmune Cord Blood Bank. AssureImmune provides regulatory consulting services and AK and XX own equity in the Organicell Regenerative Medicine.

Author Contributions

Conception and design of the study: MB, KY, AK, XX, GS, MM. Acquisition of data: MB, JM, IS, ZA, DS, AA, PC, JH, KW, KK, SS. Analysis and interpretation of data: MB, KY, JM, PC, JH. Drafting or revising the manuscript: MB, KY, MM. All authors have approved the final article.

Supplementary Materials

Supplementary material associated with this article can be found in the online version at doi:10.1016/j.jcyt.2021.07.011.

References

[1] Collins JJP, Tibboel D, de Kleer IM, Reiss IKM, Rottier RJ. The Future of Bronchopulmonary Dysplasia: Emerging Pathophysiological Concepts and Potential New Avenues of Treatment. Front Med (Lausanne) 2017;4:61.
[2] Thebaud B, Goss KN, Laughon M, Whitsett JA, Abman SH, Steinhorn RH, et al. Bronchopulmonary dysplasia. Nat Rev Dis Primers 2019;5(1):78.
[3] Belousoff MJ, Venugopal H, Wright A, Senoner S, Stuart I, Stubenrauch C, et al. CryoEM guided development of antibiotics for drug-resistant bacteria. ChemMedChem 2019;14:527.
[4] Somashekar ST, Sammour I, Huang J, Dominguez-Bendala J, Pastori R, Alvarez-Cubela S, et al. Intra-Amniotic Soluble Endoglin Impairs Lung Development in Neonatal Rats. Am J Respir Cell Mol Biol 2017;57(4):468–76.
[5] Stoll BJ, Hansen NI, Bell EF, Shankaran S, Laptook AR, Walsh MC, et al. Neonatal Outcomes of Extremely Preterm Infants From the NICHD Neonatal Research Network. Pediatrics 2010;126(3):443–56.
[6] Coalson JJ. Pathology of new bronchopulmonary dysplasia. Semin Neonatol 2003;8(1):73–81.
[7] Groothuis JR, Gutierrez KM, Lauer BA. Respiratory syncytial virus infection in children with bronchopulmonary dysplasia. Pediatrics 1988;82(2):199–203.
[8] Reiter J, Drummond S, Sammour I, Huang J, Florea V, Dornas P, et al. Stromal derived factor-1 mediates the lung regenerative effects of mesenchymal stem cells in a rodent model of bronchopulmonary dysplasia. Respir Res 2017;18(1):137.
[9] Lim R, Malhotra A, Tan J, Chan ST, Lau S, Zhu D, et al. First-In-Human Administration of Allogeneic Amnion Cells in Premature Infants With Bronchopulmonary Dysplasia: A Safety Study. Stem Cells Transl Med 2018;7(9):628–35.
[10] Burke J, Kolhe R, Hunter M, Isales C, Hamrick M, Fulzele S. Stem Cell-Derived Exosomes: A Potential Alternative Therapeutic Agent in Orthopaedics. Stem Cells Int 2016;2016:5802529.
[11] Elahi FM, Farwell DG, Nolta JA, Anderson JD. Preclinical translation of exosomes derived from mesenchymal stem/stromal cells. Stem Cells 2020;38(1):15–21.
[12] Dabrowska S, Andrzejewska A, Lukomska B, Janowski M. Neuroinflammation as a target for treatment of stroke using mesenchymal stem cells and extracellular vesicles. J Neuroinflammation 2019;16(1):178.
[13] Foster BP, Balassa T, Benen TD, Dominovic M, Elmadjian GK, Florova V, et al. Extracellular vesicles in blood, milk and body fluids of the female and male urogenital tract and with special regard to reproduction. Crit Rev Clin Lab Sci 2016;53(6):379–95.
[14] Ebert B, Rai AJ. Isolation and Characterization of Amniotic Fluid-Derived Extracellular Vesicles for Biomarker Discovery. Methods Mol Biol 2019;1885:287–94.
[15] Kosanovic M, Milutinovic B, Goc S, Mitic N, Jankovic M. Ion-exchange chromatography purification of extracellular vesicles. Biotechniques 2017;63(2):65–71.
[16] Dixon CL, Sheller-Miller S, Saade GR, Fortunato SJ, Lai A, Palma C, et al. Amniotic Fluid Exosome Proteomic Profile Exhibits Unique Pathways of Term and Preterm Labor. Endocrinology 2018;159(5):2229–40.
[17] Underwood MA, Gilbert WM, Sherman MP. Amniotic fluid: not just fetal urine anymore. J Perinatol 2005;25(5):341–8.
[18] Yet SF, Perrella MA, Layne MD, Hsieh CM, Maemura K, Kobzik L, et al. Hypoxia induces severe right ventricular dilatation and infarction in heme oxygenase-1 null mice. The Journal of clinical investigation 1999;103(8):R23–9.
[19] Barile L, Moccetti T, Marban E, Vassalli G. Roles of exosomes in cardioprotection. Eur Heart J 2017;38(18):1372–9.
[20] Williams AM, Bhatti UF, Brown JF, Biesterveld BE, Kathawate RG, Graham NJ, et al. Early single-dose treatment with exosomes provides neuroprotection and improves blood-brain barrier integrity in swine model of traumatic brain injury and hemorrhagic shock. J Trauma Acute Care Surg 2020;88(2):207–18.
[21] Ha DH, Kim HK, Lee J, Kwon HH, Park GH, Yang SH, et al. Mesenchymal Stem/Stromal Cell-Derived Exosomes for Immunomodulatory Therapeutics and Skin Regeneration. Cells 2020;9(5):1157.
[22] Porzionato A, Zaramella P, Dedja A, Guidolin D, Van Wemmel K, Macchi V, et al. Intratracheal administration of clinical-grade mesenchymal stem cell-derived extracellular vesicles reduces lung injury in a rat model of bronchopulmonary dysplasia. Am J Physiol Lung Cell Mol Physiol 2019;316(1):L6–L19.
[23] Willis GR, Fernandez-Gonzalez A, Reis M, Yeung V, Liu X, Ericsson M, et al. Mesenchymal stromal cell-derived small extracellular vesicles restore lung architecture and improve exercise capacity in a model of neonatal hyperoxia-induced lung injury. J Extracell Vesicles 2020;9(1):1790874.
[24] Willis GR, Fernandez-Gonzalez A, Anastas J, Vitali SH, Liu X, Ericsson M, et al. Mesenchymal Stromal Cell Exosomes Ameliorate Experimental Bronchopulmonary Dysplasia and Restore Lung Function through Macrophage Immunomodulation. Am J Respir Crit Care Med 2018;197(1):104–16.
[25] Colao IL, Corteling R, Bracewell D, Wall I. Manufacturing Exosomes: A Promising Therapeutic Platform. Trends Mol Med 2018;24(3):242–56.
[26] FDA. 21CFR1271, human cells, tissues, and cellular and tissue-based products. Code of Federal Regulations 2020;8 https://www.accessdata.fda.gov/scripts/cdrh/cfdocs/cfcfr/CFRSearch.cfm?CFRPart=1271&showFR=1. Accessed November , 2020.
[27] FDA. Guidance for Industry—Current Good Tissue Practice (CGTP) and Additional Requirements for Manufacturers of Human Cells, Tissues, and Cellular and Tissue-Based Products (HCT/Ps) 2011. https://www.fda.gov/regulatory-information/search-fda-guidance-documents/current-good-tissue-practice-cgtp-and-additional-requirements-manufacturers-human-cells-tissues-and. [Accessed November 2020].
[28] Gallet R, Dawkins J, Valle J, Simsolo E, de Couto G, Middleton R, et al. Exosomes secreted by cardiosphere-derived cells reduce scarring, attenuate adverse remodelling, and improve function in acute and chronic porcine myocardial infarction. Eur Heart J 2017;38(3):201–11.
[29] Zhang L, Zhu XY, Zhao Y, Eirin A, Liu L, Ferguson CM, et al. Selective intrarenal delivery of mesenchymal stem cell-derived extracellular vesicles attenuates myocardial injury in experimental metabolic renovascular disease. Basic Res Cardiol 2020;115(2):16.
[30] Koike C, Zhou K, Takeda Y, Fathy M, Okabe M, Yoshida T, et al. Characterization of amniotic stem cells. Cell Reprogram 2014;16(4):298–305.
[31] Sun Q, Li F, Li H, Chen RH, Gu YZ, Chen Y, et al. Amniotic fluid stem cells provide considerable advantages in epidermal regeneration: B7H4 creates a moderate inflammation microenvironment to promote wound repair. Sci Rep 2015;5:11560.
[32] Zhu D, Wallace EM, Lim R. Cell-based therapies for the preterm infant. Cytotherapy 2014;16(12):1614–28.
[33] Wassmer CH, Berishvili E. Immunomodulatory Properties of Amniotic Membrane Derivatives and Their Potential in Regenerative Medicine. Curr Diab Rep 2020;20(8):31.
[34] Ferguson SW, Wang J, Lee CJ, Liu M, Neelamegham S, Canty JM, et al. The microRNA regulatory landscape of MSC-derived exosomes: a systems view. Sci Rep 2018;8(1):1419.
[35] Zhao J, Li X, Hu J, Chen F, Qiao S, Sun X, et al. Mesenchymal stromal cell-derived exosomes attenuate myocardial ischaemia-reperfusion injury through miR-182-regulated macrophage polarization. Cardiovasc Res 2019;115(7):1205–16.
[36] Luther KM, Haar L, McGuinness M, Wang Y, Lynch Iv TL, Phan A, et al. Exosomal miR-21a-5p mediates cardioprotection by mesenchymal stem cells. J Mol Cell Cardiol 2018;119:125–37.
[37] Xiao C, Wang K, Xu Y, Hu H, Zhang N, Wang Y, et al. Transplanted Mesenchymal Stem Cells Reduce Autophagic Flux in Infarcted Hearts via the Exosomal Transfer of miR-125b. Circ Res 2018;123(5):564–78.
[38] Baglio SR, Rooijers K, Koppers-Lalic D, Verweij FJ, Perez Lanzon M, Zini N, et al. Human bone marrow- and adipose-mesenchymal stem cells secrete exosomes enriched in distinctive miRNA and tRNA species. Stem Cell Res Ther 2015;6:127.
[39] Nagano N, Tanaka K, Ozawa J, Watanabe T, Miyake F, Matsumura S, et al. Attenuation of Hyperoxic Lung Injury in Newborn Thioredoxin-1-Overexpressing Mice through the Suppression of Proinflammatory Cytokine mRNA Expression. Biomedicines 2020;8(3):66.
[40] El Hadri K, Mahmood DF, Couchie D, Jguirim-Souissi I, Genze F, Diderot V, et al. Thioredoxin-1 promotes anti-inflammatory macrophages of the M2 phenotype and antagonizes atherosclerosis. Arterioscler Thromb Vasc Biol 2012;32(6):1445–52.
[41] Poonyagariyagorn HK, Metzger S, Dikeman D, Mercado AL, Malinina A, Calvi C, et al. Superoxide dismutase 3 dysregulation in a murine model of neonatal lung injury. Am J Respir Cell Mol Biol 2014;51(3):380–90.
[42] Stouch AN, McCoy AM, Greer RM, Lakhdari O, Yull FE, Blackwell TS, et al. IL-1beta and Inflammasome Activity Link Inflammation to Abnormal Fetal Airway Development. Journal of immunology (Baltimore, Md: 1950) 2016;196(8):3411–20.

[43] Velten M, Heyob KM, Rogers LK, Welty SE. Deficits in lung alveolarization and function after systemic maternal inflammation and neonatal hyperoxia exposure. Journal of applied physiology (Bethesda, Md: 1985) 2010;108(5):1347–56.
[44] Jiang S, Hu Y, Deng S, Deng J, Yu X, Huang G, et al. miR-146a regulates inflammatory cytokine production in Porphyromonas gingivalis lipopolysaccharide-stimulated B cells by targeting IRAK1 but not TRAF6. Biochim Biophys Acta Mol Basis Dis 2018;1864(3):925–33.
[45] Comer BS, Camoretti-Mercado B, Kogut PC, Halayko AJ, Solway J, Gerthoffer WT. MicroRNA-146a and microRNA-146b expression and anti-inflammatory function in human airway smooth muscle. Am J Physiol Lung Cell Mol Physiol 2014;307(9):L727–34.
[46] Bobba CM, Fei Q, Shukla V, Lee H, Patel P, Putman RK, et al. Nanoparticle delivery of microRNA-146a regulates mechanotransduction in lung macrophages and mitigates injury during mechanical ventilation. Nat Commun 2021;12(1):289.